Sparse Representation-Based Inundation Depth Estimation Using SAR Data and Digital Elevation Model

Luis Moya, Erick Mas, and Shunichi Koshimura

***Abstract*—Floods increase every year worldwide, and prompt information about the affected areas is essential for early disaster response. There has been extensive development in applying remote sensing data to identify floods. In fact, remote sensing data are the only tool to identify the extent of large-scale floods within hours after their occurrence. However, few studies have addressed methods to estimate inundation depth. Inundation depth can be advantageous for identifying areas where people may need assistance during evacuation and estimating damage loss. We present a practical application of sparse representation that integrates a synthetic aperture radar-based flood binary map with a digital elevation model to estimate inundation depths. We assume that the floodwaters can be modeled as a combination of water bodies at a state of rest. A dictionary of water bodies computed under potential inundation levels is constructed from the digital elevation model. Then, the actual flood extent is represented as a sparse linear combination of the water body dictionary. The inundation depth can be estimated because each water body from the linear combination is associated with an inundation level. To assess our proposed procedure, we computed the inundation depth of the flood in the town of Mabi, Okayama Prefecture, produced during the 2018 heavy rainfall. An average absolute value difference of about 60 cm between our results and a field survey performed by a third party was observed. Two other floods produced by the 2019 Hagibis typhoon were analyzed to illustrate the relevant information that can provide inundation depths.**

***Index Terms*—Disaster resilience, floods, inundation depth, sparse representation, synthetic aperture radar (SAR).**

I. Introduction

FLOODS are defined as a large amount of water that cover areas that are usually dry. With 44% of disasters occurring between 2000 and 2019, floods are the most common type of disaster [1]. In 2020, four of the ten most expensive disasters were associated with floods [2]: China ($32 billion), India ($10 billion), Kyushu-Japan ($5 billion), and Pakistan ($1.5 billion). Similar numbers were reported in 2021 [3]: Australia ($2.1 billion), Europe ($43 billion), China ($17.6), and Canada ($7.5 billion). Several studies have shown that flood-frequency is increasing worldwide due to climate change. For instance, an increase in river floods in northwestern Europe and a reduction in southern and eastern Europe have been reported [4]. In addition, a recent study by the World Weather Attribution initiative pointed out that climate change has caused severe floods in eastern South Africa [5]. It has also been suggested that heavy rainfall, one of the triggers of floods, is very likely to occur after a wildfire [6], which may produce even more devastating effects. It is therefore relevant to consider climate change in flood risk mapping [7]. Floods cause casualties, damage infrastructure, affect agricultural activities, induce outbreaks of waterborne diseases, and contaminate drinking water. Therefore, rescue and recovery activities need to be performed as part of the early disaster response. For this purpose, a flood extent map is necessary.

Remote sensing technology is the only source of information available to map large flooded areas, and synthetic aperture radar (SAR) images are commonly used due to their ability to penetrate clouds and work at day and night. There is a vast literature on methodologies used to identify floodwaters. Most studies lie on the physical mechanism of radar backscattering in different land uses, such as flat soil, water bodies, and urban areas [8], [9], [10], [11]. A study on the effect of the satellite observation modes and orbit conditions in flood mapping was performed in [12]. Regarding the methods, backscattering intensity thresholding is the simplest, yet effective, method to identify water bodies in flat areas [13], [14]. Permanent water bodies have been used as water references to compute suitable thresholds [15]. Another novel approach consists of the use of local thresholds to the backscattering [16]. Thresholding has also been applied to the difference intensity between a pair of SAR images recorded before and after the flood occurrence [17], [18]. A decision tree was adopted in [19] to map the flood extent in the lower Amazon River. Most studies have focused on the use of single polarization SAR images. VV-polarization from the Sentinel-1 constellation, and HH-polarization from the ALOS-2 satellite are such examples. However, the use of full polarization SAR

Manuscript received 11 July 2022; revised 15 September 2022; accepted 9 October 2022. Date of publication 19 October 2022; date of current version 27 October 2022. This work was supported in part by the Japan Society for the Promotion of Science (JSPS) Kakenhi under Grant 21H05001, the Japan Science and Technology Agency (JST) Japan-US Collaborative Research Program under Grant JPMJSC2119, the Core Research Cluster of Disaster Science, the Co-creation Center for Disaster Resilience, and the Tough Cyberphysical AI Research Center at Tohoku University. (*Corresponding author: Luis Moya.*)

Luis Moya is with the GERDIS Research Group, Department of Engineering, Pontificia Universidad Católica del Perú, Lima 15088, Peru, and also with the International Research Institute of Disaster Science, Tohoku University, Sendai 980-8579, Japan (e-mail: lmoya@pucp.edu.pe).

Erick Mas and Shunichi Koshimura are with the International Research Institute of Disaster Science, Tohoku University, Sendai 980-8579, Japan (e-mail: mas@irides.tohoku.ac.jp; koshimura@irides.tohoku.ac.jp).

Digital Object Identifier 10.1109/JSTARS.2022.3215719

images is reported in [20]. Another common practice for flood mapping is the use of one post-event image and one, or two, preevent images [9], [10], [17], [21]. However, exploiting the open access of Sentinel-1 constellation, a time series analysis of backscattering using a larger number of preevent SAR images is reported in [22]. In [23], fuzzy logic was employed to map floods under vegetation from SAR images. Near real-time flood mapping based on four main steps, binary classification, morphological processing, multithreshold compensation, and machine learning-based correction, was proposed in [24]. The use of news media information to collect accurate training samples and thus identify flooded areas in near real time in proposed in [25]. In addition, it has been pointed out that manual collection of training samples is not necessary to apply machine learning to the problem of flood mapping [26]. An early estimate of the flood extent based on numerical simulations can be used to automatically collect training samples. Recent developments in flood mapping have been focused on deep learning models with special attention to multimodal deep learning and multitemporal deep learning. The term multimodal refers to data collected from multiple sensors [27], [28]. In [29], the performance of different modalities on a wide range of disasters, including floods, to identify damaged buildings was studied. The fusion of Sentinel-1 and Sentinel-2 imagery using deep learning algorithms is reported in [30] and [31].

The methodologies mentioned above have a binary map as the output product. That is, the areas are labeled flooded or nonflooded. There is, however, a strong interest in estimating the inundation depth, as it is a measure of the intensity of the disaster at a given location. For the sake of clarity, *inundation depth* refers to the vertical distance between the ground and the floodwater surface. Direct communication with the private sector has pointed out the necessity of insurance companies to estimate inundation depth within 48 h after the occurrence of a flood. This information allows them to have a better estimation of the number of claims and to adjust their resources, which would lead to prompt support for the victims. The Geospatial Information Authority (GSI) of Japan is one pioneer in providing inundation depth in recent events in the country [32], [33], [34]. GSI uses social network photographs and aerial images to map flood boundaries and identify water bodies by visual interpretation. It is assumed that the surface of a water body has a constant elevation. Note that a digital elevation model (DEM) is also required to compute inundation depths. Further details can be found in [35]. Recent efforts to replace the visual interpretation of social media images with automated algorithms to estimate inundation depth were reported in [36] and [37]. There have been few studies on the estimation of inundation depth from remote sensing. It seems unlikely that there is a possibility of estimating inundation depth solely from SAR imagery; however, an attempt is reported in [38]. More precise results were achieved by integrating remote sensing data with DEMs. The term *inundation level* is introduced here as the vertical coordinate of the floodwater surface using the same coordinate system as the DEM. In [39], a method to estimate inundation depths from a binary flood map and a DEM is proposed. First, water body boundaries are identified, and the inundation level at the boundaries is extracted from a DEM. Then, the flood inundation level at the pixels within the water bodies is assumed to be the same as the inundation level of the closest boundary pixel. Finally, the inundation depth is computed by removing the DEM from the inundation level. The accuracy of the proposed method depends highly on the accuracy of the floodwater boundaries. Unfortunately, SAR-based binary flood maps contain noise due to the speckle effect that may compromise the precision of the floodwater boundaries. Another approach divides the flood map into a number of grid areas [40]. Then, for each grid, the inundation level is assumed to be constant, and it is adjusted to fit the flood extent. Finally, the inundation level map over the whole area is computed using an interpolation technique. Note that the grid area must be large enough to estimate the inundation level. Consider, for the sake of argument, that such a grid contains only a single pixel from the DEM; then, the inundation level could be any real number greater than the DEM value in such a grid. On the other hand, a much larger area may compromise the spatial resolution of the results.

In this article, we propose the use of sparse representation to estimate inundation depths from a SAR-based binary flood map and a DEM of the affected area. We assume that the SAR-based binary map can be represented as a sparse linear combination of binary water bodies constructed from the DEM. Similar to the work reported in [40], the inundation level is fitted to construct water bodies from the DEM; however, instead of using grid areas, we adopt a sparse modeling technique to select the water bodies that conform to the whole flooded area. Finally, the set of inundation levels used to construct the selected water bodies is used to compute the inundation depths. The main contribution of the proposed methodology is twofold.

1) The flood extent is modeled as a sparse combination of a set of water bodies.
2) The proposed method can work with flood maps contaminated with noise, usually observed in SAR-based flood maps.

The rest of the manuscript is structured as follows. Section II provides the details of the proposed methodology, which covers the construction of water bodies and the mathematical formulation to identify the water bodies that conform to the actual flood extent and the computation of inundation depths. Section III reports the empirical evaluation. Here, we used the inundation depths recorded by independent research teams during the 2018 heavy rain floods in Okayama prefecture. Section IV provides a discussion of the study. Finally, Section V concludes this article.

II. Inundation Depth Estimation Method

The basis of the proposed method consists of generating a set of synthetic waterbodies from the DEM under different inundation levels. Each water body is represented as a binary map. Then, we postulate that the actual flood map, computed from SAR images, can be modeled as a sparse combination of the synthetic water bodies. Once the selected synthetic water bodies that conform to the actual flood map have been identified, the inundation depth can be computed from the inundation levels employed to create such synthetic water bodies.

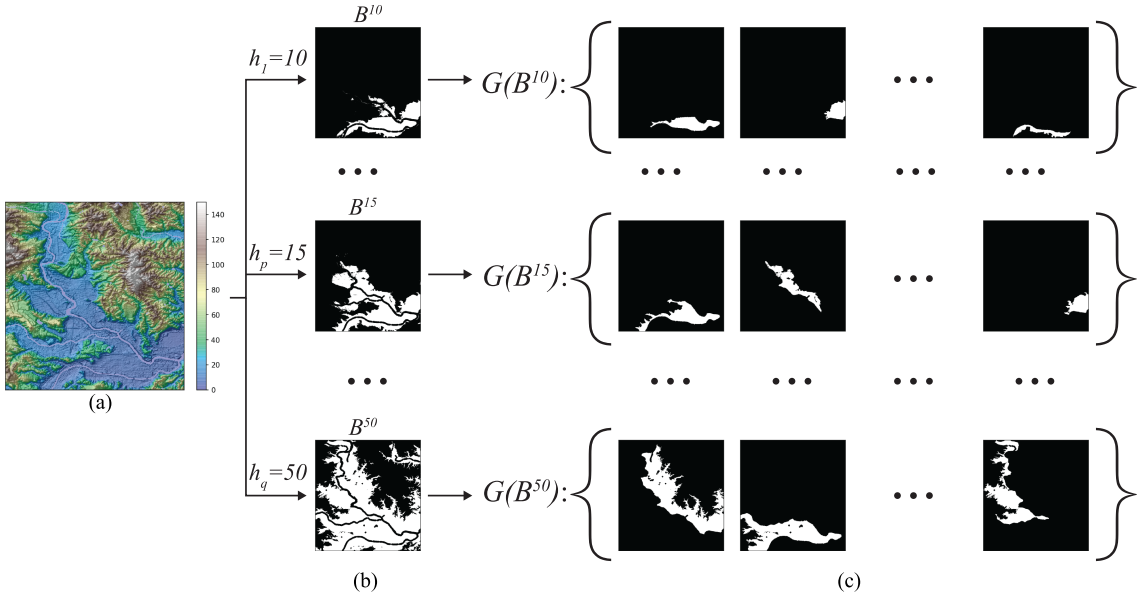

Fig. 1. Scheme of the construction of the dictionary of water bodies. First, with the aid of the DEM (a) and the set $\mathcal{H}$ of inundation levels, the set $\mathcal{B}$ of binary flood maps with constant inundation level is constructed (b). Then, the flood maps are decomposed into water bodies, or clusters, and collected into the set $\mathcal{C}$ (c).

Consider a DEM, $E \in \mathbb{R}^{m\times n}$ Fig. 1(a), and a binary image, $B \in \mathbb{V}^{m\times n}$, where $V \in \{0, 1\}$. A function $f : (\mathbb{R}^{m\times n}, \mathbb{R}) \to \mathbb{V}^{m\times n}$ to compute the flood extent that consists of all possible water bodies with a constant inundation level, h, is defined as follows:

$$f(E,h)_{i,j} = B^h_{i,j} = \begin{cases} 1 \text{ if } E_{i,j} \leq h \\ 0 \text{ otherwise.} \end{cases} \tag{1}$$

We now define the operator $G(B^h) = \{W^k\}_{k=1}^c$ as the partition of B^h into a set of clusters $\{W^k\}_{k=1}^c$, where c is the number of clusters (i.e., the cardinality of the referred set), and $W^k \in \mathbb{V}^{m\times n}$ is an array that contains a single cluster. Note that a cluster refers to a group of neighboring pixels with $W^k_{i,j} = 1$. Here, pixels are referred to as neighbors if they have one side in common. In the specific context of this study, a cluster represents a water body.

Consider that $\mathcal{H} = \{h_1, \ldots, h_n\}$ is a set of potential inundation levels, the set $\mathcal{B} = \{B^h | B^h = f(E, h); h \in \mathcal{H}\}$ denotes a set of binary flood maps computed from each element of $\mathcal{H}$ Fig. 1(b), and the set $\mathcal{C} = \{W^i | W^i \in G(B), B \in \mathcal{B}\}$ denotes the water bodies (clusters) constructed from the binary images of $\mathcal{B}$ Fig. 1(c). Let us denote B^* an arbitrary real flood map. We consider that B^* can be represented as a linear combination of the components of $\mathcal{C}$:

$$\mathbf{Ax} = \mathbf{b} \tag{2}$$

where $\mathbf{b} \in \mathbb{V}^{mn}$ denotes B^* in a vector format, $\mathbf{A} \in \mathbb{V}^{mn\times s}$ is a matrix with mn rows and s columns, where s is the cardinality of $\mathcal{C}$, and $\mathbf{x} \in \mathbb{V}^{mn}$ is a vector whose components are either one or zero. Note that the k-column of $\mathbf{A}$, hereafter referred to as $\mathbf{a}_k$, is an element of $\mathcal{C}$ in vector format. An additional assumption is that $\mathbf{x}$ is sparse. Then, (2), and the additional constraints can be expressed as an optimization problem

$$\begin{aligned} &\min_{\mathbf{x}} ||\mathbf{x}||_0 \\ &\text{subject to } \mathbf{Ax} = \mathbf{b} \\ &\mathbf{x}_i \in \mathbb{V} \end{aligned} \tag{3}$$

where $||\mathbf{x}||_0$ denotes the l_0-norm. That is, the number of nonzero components of $\mathbf{x}$. (3) denotes a nonlinear programming problem, often denoted as the P_0-problem. A support vector of the P_0-problem is the vector $\mathbf{a}_k$ such that $\mathbf{x}_k = 1$. We introduce the set $\mathcal{S} = \{k | \mathbf{x}_k = 1\}$ as the set of the indices of all support vectors. Another condition that we exploit is that the support vectors are orthogonal. That is, for any two support vectors, $\mathbf{a}^i$ and $\mathbf{a}^j$, $\mathbf{a}_i^T \mathbf{a}_j = 0$. A violation of these conditions indicates that some areas of a water body have been counted twice. Then, we can solve the P_0-problem using greedy algorithms, a number of techniques that only work under specific conditions, such as our case.

In this study, we adopt the orthogonal-matching pursuit (OMP) algorithm, with practical simplifications based on the nature of the problem, to solve (3). Further details on the OMP algorithm can be found in [41]. The initialization of the OMP algorithm is as follows.

1) The initial solution $\mathbf{x}^0 = \mathbf{0}$.
2) The initial residual $\mathbf{r}^0 = \mathbf{b} - \mathbf{Ax}^0 = \mathbf{b}$.
3) The initial solution support $\mathcal{S}^0 = \emptyset$.

Then, the following steps are repeated with increments of k by one:

1) *Sweep:* Compute the errors $\epsilon(j) = \|\mathbf{a}_j - \mathbf{r}^{k-1}\|_2^2$ for all j.
2) *Update support:* Find a minimizer, j_0 of $\epsilon(j) : \forall j \notin \mathcal{S}^{k-1}$, $\epsilon(j_0) \leq \epsilon(j)$, and update $\mathcal{S}^k = \mathcal{S}^{k-1} \cup \{j_0\}$.

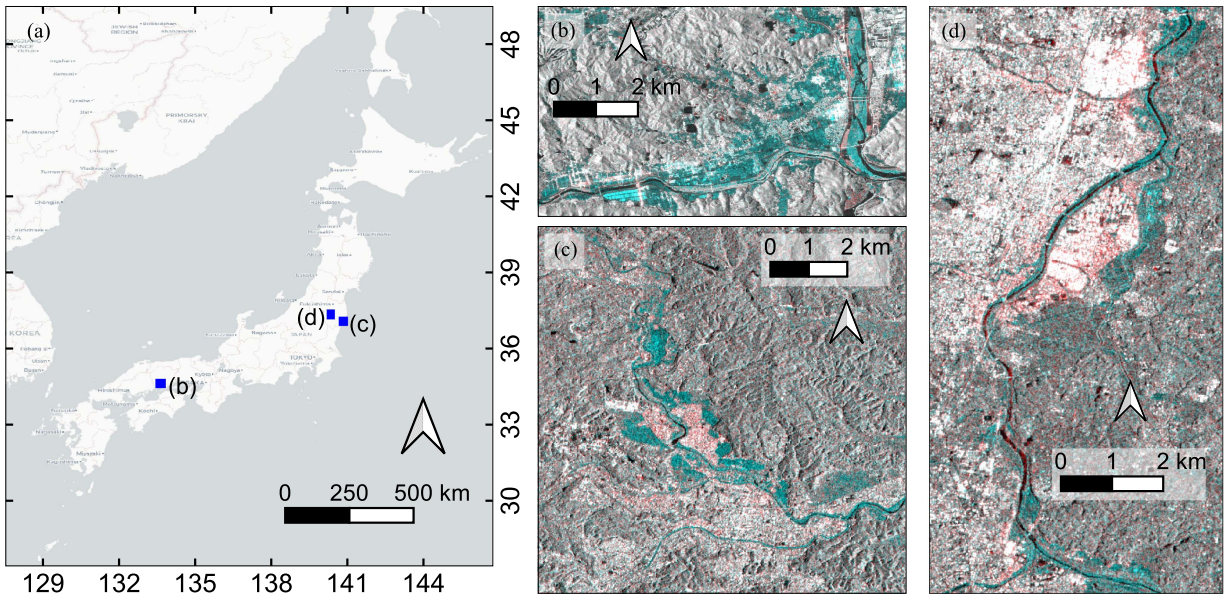

Fig. 2. Study cases for the experimental evaluation. (a) Location of study cases in Japan. Color composite (i.e., red band: post-event image; and green and blue band: preevent image) of SAR backscattering intensity at (b) the town of Mabi, (c) the city of Iwaki, and (d) the city of Koriyama.

3) *Update provisional solution:* Update $\mathbf{x}$ such that $\mathbf{x}_j = 1$ if $j \in \mathcal{S}^k$, otherwise $\mathbf{x}_j = 0$.
4) *Update residual:* $\mathbf{r}^k = \mathbf{b} - \mathbf{A}\mathbf{x}^k$.
5) *Stopping rule:* If $\|\mathbf{r}^{k-1}\|_2 - \|\mathbf{r}^k\|_2 < \epsilon_0$, stop iteration. Otherwise, apply another iteration.

Once (3) is solved, the inundation level $h \in \mathcal{H}$ used to construct each support vector can be retrieved. Recall that the support vector is merely a binary water body in vector format. Finally, the inundation depth is computed as the difference between the inundation level and the DEM within the water body.

III. Experimental Evaluation

This section reports some applications of the methodology on flood maps computed from SAR images. Three affected areas in Japan, the town of Mabi, the city of Iwaki and the city of Koriyama, are selected as case studies Fig. 2(a). The results in the town of Mabi are compared with information collected from field surveys, and thus, a quantitative evaluation of the accuracy is performed. The other two cases are used to point out the information that can be retrieved from inundation depths. For each case study, three SAR images were employed to compute the flood extent, one image recorded after the flood event and two images recorded before. For preprocessing of the SAR data, radiometric calibration, speckle filtering, multilooking, and terrain correction were applied to obtain the SAR backscattering intensity. Fig. 2(b)–(d) depict the color composite image of the SAR backscattering intensity. The red band denotes the SAR image recorded after the flood occurrence, hereafter referred to as a postevent image. The green and blue bands denote a SAR image recorded before the flood occurrence, hereafter referred to as a preevent image. The cyan tones denote a reduction in the time of the backscattered intensity, whereas red tones show increases. In addition to the backscattering intensity, the interferometric coherence is computed from multitemporal SAR data. The interferometric coherence computed from a postevent and a preevent image is referred to as coevent coherence. Likewise, the interferometric coherence computed from two preevent images is referred to as preevent coherence. The methods adopted to obtain the flood map are reported in the following subsections.

Some words regarding the definition of $\mathcal{H}$ are necessary. An arithmetic sequence, $h_n = h_{n-1} + d$, is used to define the elements of $\mathcal{H}$. We consider $d = 10291\ cm$ to be a practical choice. Recall that due to speckle noise, a SAR-based flood extent map exhibits a certain level of noise. Thus, h_0 is defined as the smallest value such that 5% of the pixels classified as flooded in B^* have an elevation lower than h_0. Likewise, the last element of $\mathcal{H}$, h_n, is defined as the smallest value such that 95% of the pixels classified as flooded in B^* have an elevation lower than h_n. Furthermore, to reduce the computational load, water bodies in $\mathcal{C}$ with sizes lower than or equal to 4 pixels were filtered out.

A. 2018 Mabi, Okayama Flood

On July 5, 2018, a weather front moved to western Japan, and approximately the same time, Typhoon Prapiroon approached the country. As a result, continuous supply of warm and very moist air induced a record-breaking rainfall that led to several floods. A total of 237 casualties were reported in [43]. The town of Mabi was one of the severely affected areas. The flood extent, $\mathcal{B}^*$, was constructed by merging the flood map in nonurban and urban areas that was reported in [9] Fig. 3(b). The floods in nonurban areas were computed by thresholding the backscattering intensity using a threshold of -16 dB. The threshold was estimated from samples of water bodies extracted

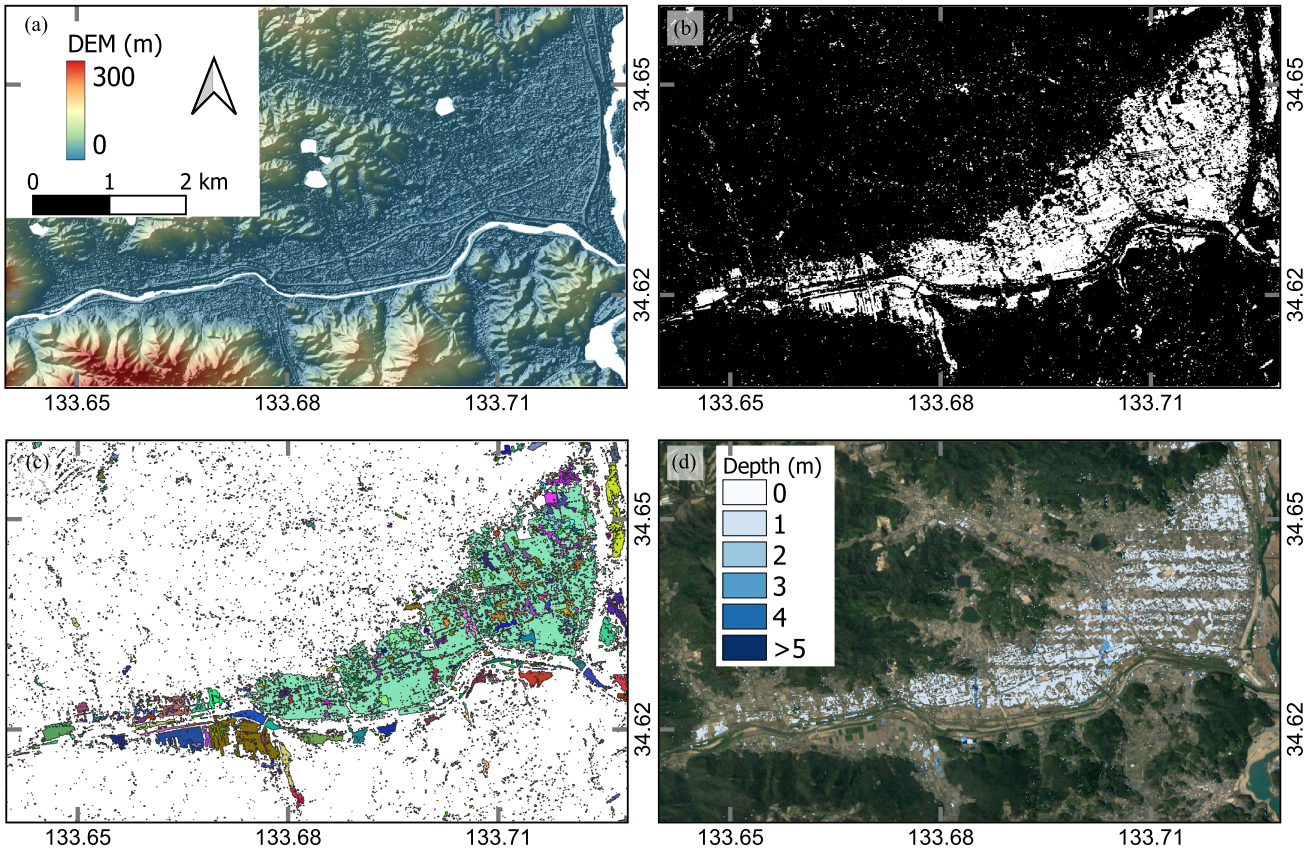

Fig. 3. Town of Mabi. (a) DEM. (b) Binary flood map, $\mathcal{B}^*$. (c) Polygons delineating the flood extent. (d) Flood inundation depth computed with the ArcGISProTool provided in [42], which is based on the method proposed in [39].

within rivers. The floods in urban areas were computed using a one-class support vector machine (SVM) classifier, from which the conditional coherence, a parameter proposed in [9], was used as the input feature. Note that the binary flood map exhibit a high noise level due to the speckle noise and shadow effects in SAR images. As a result, the polygons delineating the flood extent look fragmented, with some polygons containing other polygons inside Fig. 3(c). Recall that the method proposed in [39] assumes that the polygon's boundaries have inundation depth equal to zero and the closest pixels share the same inundation height. Under these conditions, the estimated flood inundation depth exhibits significant errors Fig. 3(d). The DEM was provided by the GSI [44], and was computed from airborne Lidar data, and has a spatial resolution of 5 m Fig. 3(a). Note that the elevation along the river and other water bodies is missing. The elevation along the river changes very frequently due to sediment transportation, and thus, the elevation during the occurrence of the flood and the acquisition date of the lidar data might be significantly different. To avoid these inconsistencies, the river shape was expanded by performing the morphological operator *dilation* six times.

Regarding the water body dataset, the set $\mathcal{H} = \{5.6\,m, 5.7\,m, \ldots, 23.4\,m\}$ was used. The cardinality of $\mathcal{C}$ (i.e., the number of columns of $\mathbf{A}$ and the number of water bodies) was 11 556. Fig. 4 depicts the outcomes of the OMP algorithm. Fig. 4(a) shows the water bodies associated with the first eight support vectors, and Fig. 4(b) shows their associated inundation level. Note that the first support vector was associated with the largest water body, the second largest with the second support vector, and so on. The evolution of the residual, $\mathbf{r}$, through the iteration process is depicted in Fig. 5(a). It is worth noting that although a convergence is achieved in the iterative processing, the residuals did not reach to zero. The main reason for this was the presence of speckle noise in the binary flood map. Fig. 4(c) depicts the estimated inundation depth. Black circle marks represent the location of field survey measurements of the inundation depth. The field survey data were reported in [45], hereafter referred to as survey A. Fig. 5(b) shows the comparison of the OMP-based inundation depth and that collected from the field survey A. As can be observed, there is good agreement between our estimations and the survey A. The average absolute value error is 60 cm. The correlation between our results and survey A is 0.80. Note that the method proposed in [38] achieved a correlation of 0.68. Another field survey measurement is reported in [46], hereafter referred to as survey B [see Fig. 4(c)]. Survey B grouped the measurements in ranges. White square marks denote measurements of inundation depth lower than 1 m; blue square marks denote inundation depth between 1 m and 2 m; green square marks between 2 m and 3 m; yellow square marks between 3 m and 4 m; orange square marks between 4 m and 5 m; and magenta square marks between 5 m and 6 m. There is also a remarkable consistency between survey B measurements and

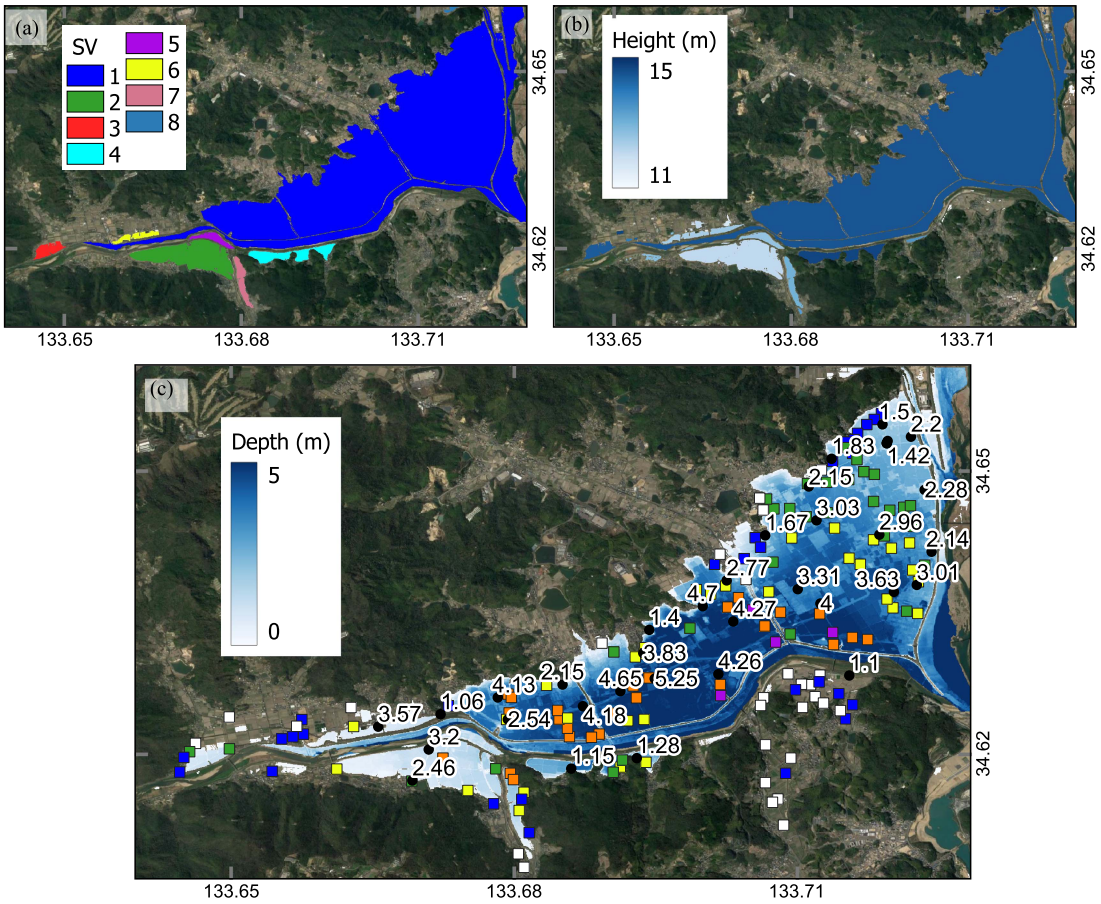

Fig. 4. Results of the case study. (a) Support vectors, (b) inundation level of the water bodies, and (c) inundation depth. Black circle marks in (c) denotes the location of the measurements from survey A, and square marks denotes the location of the measurements from survey B.

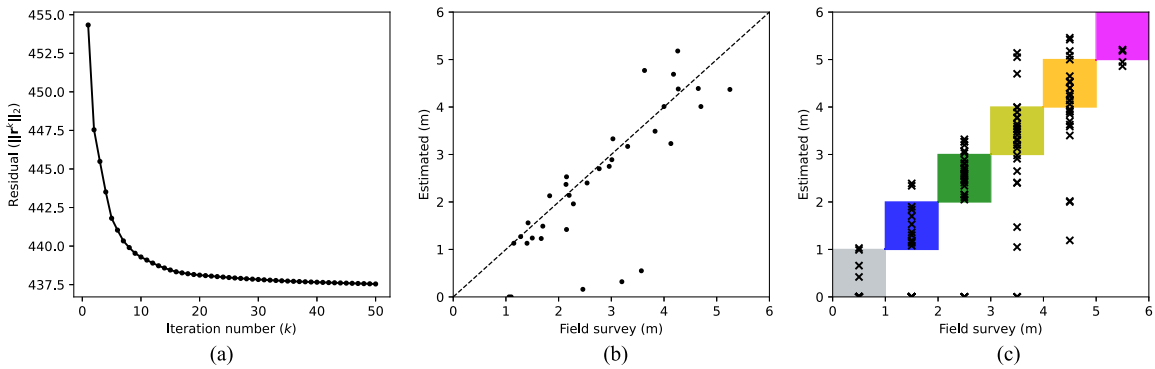

Fig. 5. (a) Variation of the residual, **r**, during the iterative process of the OMP algorithm. (b) Comparison of the inundation depth estimated from the proposed method and that measured from a field survey A. (c) Comparison of the inundation depth estimated from the proposed method and that measured from a field survey B.

our results, as shown in Fig. 5(c). Unfortunately, a quantitative evaluation was not performed due to the resolution of the survey B measurements.

B. 2019 Hagibis Typhoon

On October 12, 2019, at night, Typhoon Hagibis landed on Izu Peninsula, Japan, passed through the Kanto region, and left the country from the Tohoku region before dawn on October 13, 2019. The typhoon induced several floods in eastern Japan. As of April 10, 2020, 104 casualties, 3 missing, and 384 injured people were reported by the Government of Japan [47]. Here we estimate the inundation depth in the city of Koriyama, and the city of Iwaky. The flood extent was estimated from Sentinel-1 SAR images recorded on September 24, October 6, and October 12 of 2019. Note that the time zone in Japan is UTC+9, and

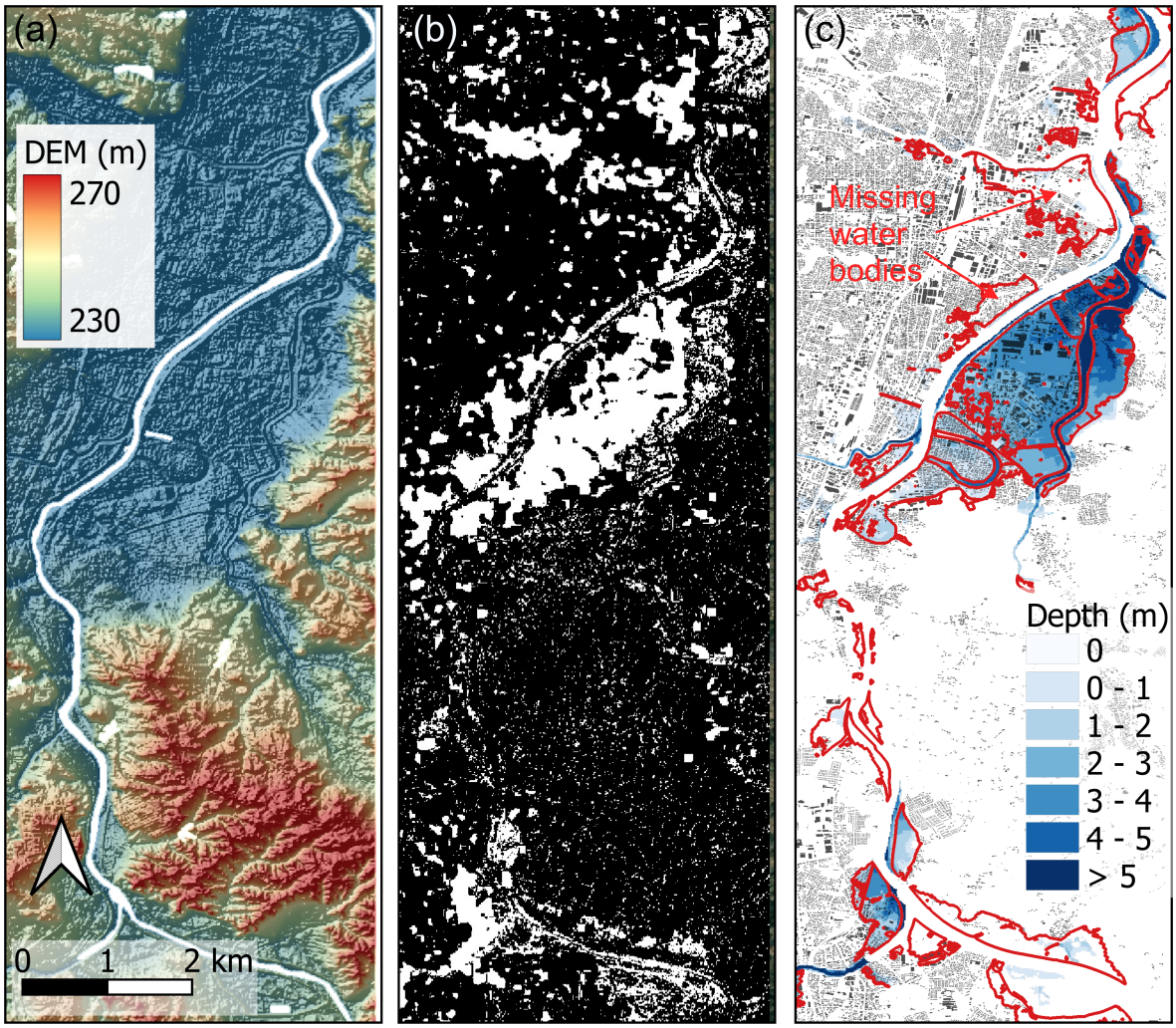

Fig. 6. City of Koriyama. (a) DEM. (b) SAR-based flood binary map. (c) OMP-based inundation depth in white-blue tones; GSI-based flood extent as red polygons; and building footprint as black polygons.

thus, the image recorded on October 12 was taken after Hagibis left Japan. Regarding the binary flood map, $\mathcal{B}^*$ is constructed by merging a flood map in urban and nonurban areas Figs. 6(b) and 7(b). The flood in urban areas reported in [10], who used a two-class SVM classifier with a preevent coherence and a coevent coherence as input features, was used in this study. The thresholding of backscattering intensity approach was used to identify floodwaters in nonurban areas. The threshold value, -16.5 dB, was set from samples of permanent water bodies from rivers. As in the previous study, the DEM was provided by the GSI [44] [see Figs. 6(a) and 7(a)]. Elevations along the river and other water bodies are missing, and their shapes were expanded using the morphological operator dilation six times.

Regarding the cities of Koriyama and Iwaki, inundation depths were estimated using the proposed method Figs. 6(c) and 7(c). The identified water bodies are consistent with the flood extent map provided in [33] and the Mayor of Iwaki city. However, some water bodies were not identified because they were absent in the flood extent map estimated from SAR data. An interesting outcome is that the speckle noise effects in the flood map extent are almost negligible in the inundation depth map. The affected areas have a detailed geocoded inventory of the building stock Figs. 6(c) and 7(c), which can be used to grasp more details regarding the affected buildings Fig. 8. In Koriyama city, a total of 6932 buildings were flooded to an inundation depth of at least 20 cm. There were 6693 affected buildings with two floors, from which the floodwaters reached the first floor of 5153 buildings, the second floor of 1531 buildings, and 9 buildings were completely flooded. Regarding buildings with three floors, 174 buildings were affected. The floodwaters reached the first floor of 146 buildings, and the second floor of 28 buildings. There were also 64 buildings with more than three floors, of which 54 were flooded to the first floor, and 10 buildings were flooded to the second floor. In the city of Iwaki, 4644 buildings were affected by the flood. There were 4566 buildings with two floors, from which 3596 buildings were affected by the floodwaters only to the first floor, 880 buildings were affected on both floors, and 90 buildings were completely covered by the floodwaters. Fifty of the affected buildings consisted of three floors, from which the floodwaters reached the first floor of 38 buildings, the second

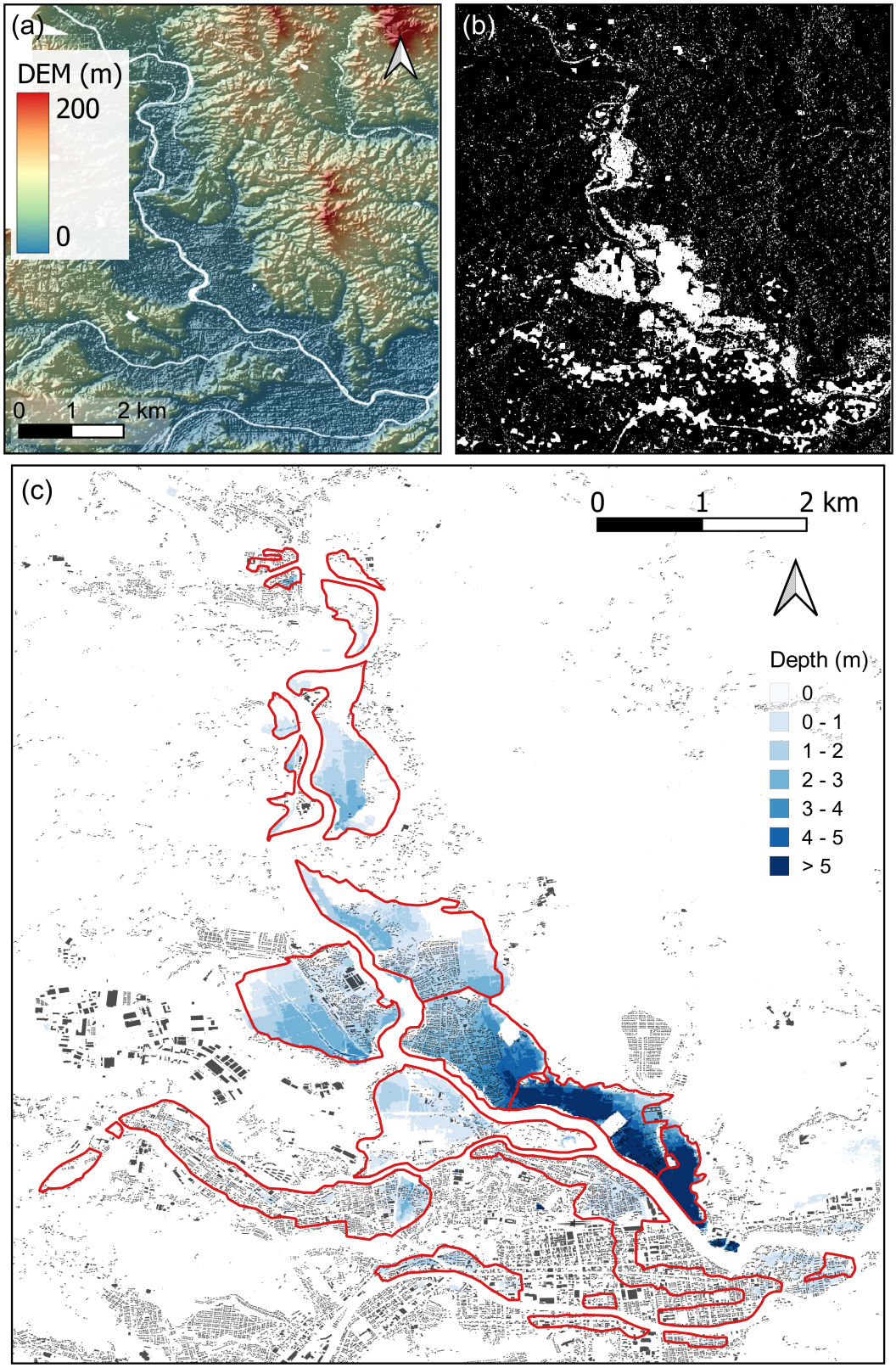

Fig. 7. Town of Iwaki. (a) DEM. (b) SAR-based binary flood map. (c) OMP-based inundation depth in white-blue tones; local government-based flood extent as red polygons; and building footprint as black polygons.

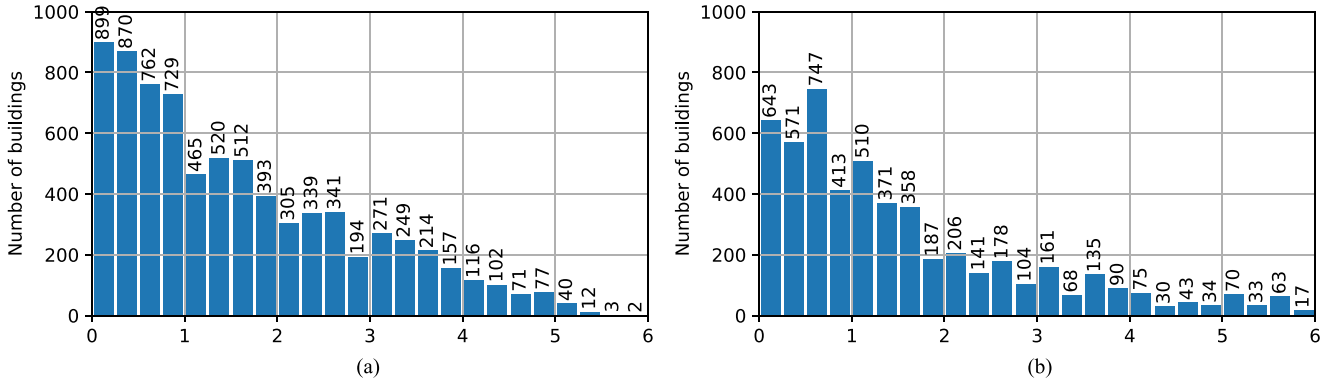

Fig. 8. Number of affected buildings per interval of inundation depth of 25 cm.

floor of 8 buildings, and the third floor of 4 buildings. In addition, there were 28 buildings with more than three floors, out of which 23 buildings were affected only to the first floor, 4 buildings were affected to the two first floors, and one building was affected to the third floor.

IV. Discussion

In this study, we adapted the OMP algorithm, reported in [41], to estimate the inundation depth. The OMP algorithm is regarded as one of the simplest approaches for sparse representation, and it only works under specific conditions. We showed that our study is one of these cases. One of the modifications concerns the sweep step of the iterative process, and the standard OMP algorithm has two targets: 1) the identification of the support vectors; 2) the nonzero values of $\mathbf{x}$. However, in our problem, it is known in advance that the nonzero values are all ones. Thus, the sweep step of the original OMP-algorithm.

Sweep: Compute the errors $\epsilon(j) = \min_{z_j} \|\mathbf{a}_j z_j - \mathbf{r}^{k-1}\|_2^2$ for all j using the optimal choice $z_j^* = \mathbf{a}_j^T \mathbf{k}^{k-1} / \|\mathbf{a}\|_2^2$ is replaced with (section II).

Sweep: Compute the errors $\epsilon(j) = \|\mathbf{a}_j - \mathbf{r}^{k-1}\|_2^2$ for all j.

This simplification significantly reduces the computational load. Another modification in our OMP-algorithm lies in the stopping rule. In the standard OMP algorithm, the stopping rule is:

Stopping rule: If $\|\mathbf{r}^k\|_2 < \epsilon_0$, stop iteration. Otherwise, apply another iteration.

There are two reasons why our approach does not guarantee that $\|\mathbf{r}^k\|$ will converge to a value lower than ϵ_0, as shown in Fig. 5. First, the columns of $\mathbf{A}$ do not necessarily contain a subset of vectors that constitute a basis for a vector space in R^{mn}. That is, not all images of size $m \times n$ can be expressed as a linear combination of the columns of $\mathbf{A}$. However, the procedure ensures that water bodies in a state of rest can be represented from a linear combination of $\mathbf{A}$. Second, the SAR-based binary flood map contains salt-and-pepper noise Figs. 3(b), 6(b), and 7(b), produced by the speckle noise effect in SAR images, which cannot be represented by a linear combination of $\mathbf{A}$. Therefore, the stopping rule has been modified to:

Stopping rule: If $\|\mathbf{r}^k\|_2 - \|\mathbf{r}^{k-1}\|_2 < \epsilon_0$, stop iteration. Otherwise, apply another iteration.

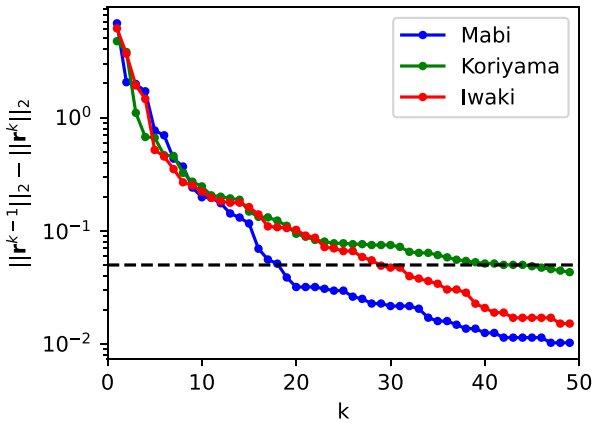

Fig. 9. Difference in the residual module between consecutive steps of the OMP algorithm, $\|\mathbf{r}^{k-1}\|_2 - \|\mathbf{r}^k\|_2$, for the first 50 iterations. The blue, green, and red lines denote the values for Mabi town, Koriyama city, and Iwaki city, respectively. The black dashed line is drawn at $\|\mathbf{r}^{k-1}\|_2 - \|\mathbf{r}^k\|_2 = 0.05$.

A value of $\epsilon_0 = 0.05$ guarantees that all water bodies in the binary flood map will be represented by a support vector of $\mathbf{A}$ Fig. 9.

In the experimental evaluation of the proposed method, we used a set of evenly spaced inundation levels with 10-cm spacing between values. The average absolute value error increased from 60 cm to 70 cm, 71 cm, 71 cm, and 74 cm when the spacing between values increased to 20 cm, 30 cm, 40 cm, and 50 cm, respectively.

Regarding runtime performance, our proposed method was implemented in the Python programming language, version 3.7 [48]. The Numerical Python library was used to vectorize the calculations [49]. The results reported in this manuscript were performed on a MacBook Pro with an Apple M1 Pro Chip. The runtime depends mainly on the number of support vectors required to represent the flood binary map. Identifying a support vector took about 30 s, 54 s, and 50 s for the floods in Mabi, Koriyama, and Iwaki, respectively. Therefore, according to Fig. 9, the estimation of inundation depth took 9 min, 40 min, and 24 min, respectively. It is worth mentioning that the runtime can still be significantly reduced as the algorithm can be implemented with parallel programming in a compiled language, such as C++ or Fortran.

V. Conclusion

We proposed a novel approach to estimate inundation depth from a flood extent map and a DEM. The main assumption of the method is that the water bodies are in a state of rest, and that the flood extent can be represented by a sparse combination of a set of water bodies constructed from the DEM. SAR-based flood binary maps were mainly employed in this study. A comparison with a field survey performed by a third party achieved an average absolute value error of 60 cm. With such a level of accuracy, it is possible to segregate buildings according to their level of damage. For instance, it is possible to group buildings according to the number of affected floors, which reflects the damage level. Furthermore, buildings that were not completely flooded can be targeted as priorities for activities associated with the search and rescue of survivors. As an unexpected characteristic, the methodology removes the speckle-based noise present in the flood binary map. It is worth mentioning that the accuracy of the results depends on the quality of the binary flood map. The accuracy also depends on the variable $\mathcal{H}$ (i.e., the set of inundation levels used to construct the water body dictionary). In this study we used a set of evenly spaced inundation heights with 10 cm spacing between values. A lower space between values may lead to more accurate results, but at the expense of a larger runtime.

References

[1] CRED and UNDRR, "The human cost of disasters: An overview of the last 20 years 2000–2019," 2020. Accessed: Apr. 8, 2021. [Online]. Available: https://www.preventionweb.net/publications/view/74124

[2] K. Kramer and J. Ware, "Counting the cost 2020: A year of climate breakdown," 2020. Accessed: Oct. 20, 2022. [Online]. Available: https://reliefweb.int/report/world/counting-cost-2020-year-climate-breakdown-december-2020

[3] K. Kramer and J. Ware, "Counting the cost 2021: A year of climate breakdown," 2021. Accessed: Oct. 20, 2022. [Online]. Available: https://reliefweb.int/report/world/counting-cost-2021-year-climate-breakdown-december-2021

[4] G. Blöschl et al., "Changing climate both increases and decreases European river floods," *Nature*, vol. 573, pp. 108–111, 2019.

[5] *World Weather Attribution*, "Climate change-exacerbated rainfall causing devastating flooding in eastern South Africa," 2022. Accessed: May 20, 2022. [Online]. Available: https://www.worldweatherattribution.org/climate-change-exacerbated-rainfall-causing-devastating-flooding-in-eastern-south-africa/

[6] D. Touma, S. Stevenson, D. L. Swain, D. Singh, D. A. Kalashnikov, and X. Huang, "Climate change increases risk of extreme rainfall following wildfire in the western United States," *Sci. Adv.*, vol. 8, no. 13, 2022, Art. no. eabm0320.

[7] O. E. J. Wing et al., "Inequitable patterns of US flood risk in the anthropocene," *Nature Climate Change*, vol. 12, pp. 156–162, 2022.

[8] Y. Li, S. Martinis, M. Wieland, S. Schlaffer, and R. Natsuaki, "Urban flood mapping using SAR intensity and interferometric coherence via Bayesian network fusion," *Remote Sens.*, vol. 11, no. 19, 2019, Art. no. 2231.

[9] L. Moya, Y. Endo, G. Okada, S. Koshimura, and E. Mas, "Drawback in the change detection approach: False detection during the 2018 western Japan floods," *Remote Sens.*, vol. 11, no. 19, 2019, Art. no. 2320.

[10] L. Moya, E. Mas, and S. Koshimura, "Learning from the 2018 western Japan heavy rains to detect floods during the 2019 hagibis typhoon," *Remote Sens.*, vol. 12, no. 14, 2020, Art. no. 2244.

[11] L. Pulvirenti, G. Squicciarino, E. Fiori, L. Ferraris, and S. Puca, "A tool for pre-operational daily mapping of floods and permanent water using sentinel-1 data," *Remote Sens.*, vol. 13, no. 7, 2021, Art. no. 1342.

[12] R. Natsuaki and H. Nagai, "Synthetic aperture radar flood detection under multiple modes and multiple orbit conditions: A case study in Japan on typhoon hagibis," 2019, *Remote Sens.*, vol. 12, no. 6, 2020, Art. no. 903.

[13] M. Ohki et al., "Flood area detection using palsar-2 amplitude and coherence data: The case of the 2015 heavy rainfall in Japan," *IEEE J. Sel. Topics Appl. Earth Observ. Remote Sens.*, vol. 12, no. 7, pp. 2288–2298, Jul. 2019.

[14] J. Zhao, R. Pelich, R. Hostache, P. Matgen, W. Wagner, and M. Chini, "A large-scale 2005–2012 flood map record derived from envisat-asar data: United kingdom as a test case," *Remote Sens. Environ.*, vol. 256, 2021, Art. no. 112338.

[15] P. Nakmuenwai, F. Yamazaki, and W. Liu, "Automated extraction of inundated areas from multi-temporal dual-polarization radarsat-2 images of the 2011 central Thailand flood," *Remote Sens.*, vol. 9, no. 1, 2017, Art. no. 78.

[16] J. Liang and D. Liu, "A local thresholding approach to flood water delineation using sentinel-1 SAR imagery," *ISPRS J. Photogrammetry Remote Sens.*, vol. 159, pp. 53–62, 2020.

[17] W. Liu, K. Fujii, Y. Maruyama, and F. Yamazaki, "Inundation assessment of the 2019 typhoon hagibis in Japan using multi-temporal sentinel-1 intensity images," *Remote Sens.*, vol. 13, no. 4, 2021, Art. no. 639.

[18] M. Singha et al., "Identifying floods and flood-affected paddy rice fields in Bangladesh based on sentinel-1 imagery and Google earth engine," *ISPRS J. Photogrammetry Remote Sens.*, vol. 166, pp. 278–293, 2020.

[19] A. S. Arnesen et al., "Monitoring flood extent in the lower amazon river floodplain using ALOS/PALSAR Scansar images," *Remote Sens. Environ.*, vol. 130, pp. 51–61, 2013.

[20] H. Sui, K. An, C. Xu, J. Liu, and W. Feng, "Flood detection in PolSAR images based on level set method considering prior geoinformation," *IEEE Geosci. Remote Sens. Lett.*, vol. 15, no. 5, pp. 699–703, May 2018.

[21] W. Liu and F. Yamazaki, "Review article: Detection of inundation areas due to the 2015 Kanto and Tohoku torrential rain in Japan based on multi-temporal ALOS-2 imagery," *Natural Hazards Earth Syst. Sci.*, vol. 18, no. 7, pp. 1905–1918, 2018.

[22] B. DeVries, C. Huang, J. Armston, W. Huang, J. W. Jones, and M. W. Lang, "Rapid and robust monitoring of flood events using sentinel-1 and landsat data on the Google earth engine," *Remote Sens. Environ.*, vol. 240, 2020, Art. no. 111664.

[23] S. Grimaldi, J. Xu, Y. Li, V. Pauwels, and J. Walker, "Flood mapping under vegetation using single SAR acquisitions," *Remote Sens. Environ.*, vol. 237, 2020, Art. no. 111582.

[24] X. Shen, E. N. Anagnostou, G. H. Allen, G. Robert Brakenridge, and A. J. Kettner, "Near-real-time non-obstructed flood inundation mapping using synthetic aperture radar," *Remote Sens. Environ.*, vol. 221, pp. 302–315, 2019.

[25] G. Okada, L. Moya, E. Mas, and S. Koshimura, "The potential role of news media to construct a machine learning based damage mapping framework," *Remote Sens.*, vol. 13, no. 7, 2021, Art. no. 1401.

[26] L. Moya, C. Geiß, M. Hashimoto, E. Mas, S. Koshimura, and G. Strunz, "Disaster intensity-based selection of training samples for remote sensing building damage classification," *IEEE Trans. Geosci. Remote Sens.*, vol. 59, no. 10, pp. 8288–8304, Oct. 2021.

[27] D. Hong et al., "More diverse means better: Multimodal deep learning meets remote-sensing imagery classification," *IEEE Trans. Geosci. Remote Sens.*, vol. 59, no. 5, pp. 4340–4354, May 2021.

[28] D. Hong, J. Hu, J. Yao, J. Chanussot, and X. X. Zhu, "Multimodal remote sensing benchmark datasets for land cover classification with a shared and specific feature learning model," *ISPRS J. Photogrammetry Remote Sens.*, vol. 178, pp. 68–80, 2021.

[29] B. Adriano et al., "Learning from multimodal and multitemporal earth observation data for building damage mapping," *ISPRS J. Photogrammetry Remote Sens.*, vol. 175, pp. 132–143, 2021.

[30] Y. Bai et al., "Enhancement of detecting permanent water and temporary water in flood disasters by fusing sentinel-1 and sentinel-2 imagery using deep learning algorithms: Demonstration of sen1floods11 benchmark datasets," *Remote Sens.*, vol. 13, no. 11, 2021, Art. no. 2220. [Online]. Available: https://www.mdpi.com/2072-4292/13/11/2220

[31] S. Martinis, S. Groth, M. Wieland, L. Knopp, and M. Rättich, "Towards a global seasonal and permanent reference water product from sentinel-1/2 data for improved flood mapping," *Remote Sens. Environ.*, vol. 278, 2022, Art. no. 113077.

[32] GSI, "Information about heavy rain in July 2018," 2018. Accessed: Jul. 19, 2019. [Online]. Available: https://www.gsi.go.jp/BOUSAI/H30.taihuu7gou.html

[33] GSI, "Information about Typhoon No. 19," 2019. Accessed: Oct. 25, 2019. [Online]. Available: https://www.gsi.go.jp/BOUSAI/R1.taihuu19gou.html
[34] GSI, "Information on heavy rain in July 2nd, 2020," 2020. Accessed: Apr. 2, 2021. [Online]. Available: https://www.gsi.go.jp/BOUSAI/R2_kyusyu_heavyrain_jul.html
[35] K. Yoshida, "Provisional inundation depth map in the heavy rain event of Jul. 2018," in *Proc. Bull. GSI*, 2019, vol. 132, pp. 17–21.
[36] P. Chaudhary, S. D'Aronco, J. Leitão, K. Schindler, and J. Wegner, "Water level prediction from social media images with a multi-task ranking approach," *ISPRS J. Photogrammetry Remote Sens.*, vol. 167, pp. 252–262, 2020.
[37] Y. Feng, C. Brenner, and M. Sester, "Flood severity mapping from volunteered geographic information by interpreting water level from images containing people: A case study of hurricane harvey," *ISPRS J. Photogrammetry Remote Sens.*, vol. 169, pp. 301–319, 2020.
[38] H. Gokon, S. Koshimura, and K. Meguro, "Estimating tsunami inundation depth using TerraSAR-X data," in *Proc. IEEE Int. Geosci. Remote Sens. Symp.*, 2019, pp. 4845–4848.
[39] S. Cohen et al., "Estimating floodwater depths from flood inundation maps and topography," *JAWRA J. Amer. Water Resour. Assoc.*, vol. 54, no. 4, pp. 847–858, 2018.
[40] C. Huang et al., "Integration of remotely sensed inundation extent and high-precision topographic data for mapping inundation depth," in *Proc. Third Int. Conf. Agro-Geoinform.*, 2014, pp. 1–4.
[41] M. Elad, *Sparse and Redundant Representations: From Theory to Applications in Signal and Image Processing*, 1st ed. Berlin, Germany: Springer, 2010.
[42] Surface Dynamics Modeling Lab, "Floodwater depth estimation tool (FwDET)," Accessed: Sep. 9, 2022. [Online]. Available: https://sdml.ua.edu/models/fwdet
[43] M. Ohara and N. Nagumo, "Mortality by age group and municipality in the Jul. 2018 torrential rainfall," *J. Disaster Res.*, vol. 14, no. 6, pp. 912–921, 2019.
[44] GSI, "Basic map information of digital elevation model," Accessed: May 1, 2022. [Online]. Available: https://fgd.gsi.go.jp/download/ref_dem.html
[45] W. Fujimoto, R. Hisamatsu, K. Kawabe, W. Echizenya, Y. Shinozuka, and K. Horie, "Simulation of the Kurashiki-Mabi flood caused by the heavy rain in Jul. Heisei 30 for estimating flood damage function," in *Proc. Annu. Conf., Jpn Soc. Hydrol. Water Resour.*, vol. 32, 2019, Art. no. 248.
[46] Y. Nihei et al., and, "Flooding along Oda river due to the western Japan heavy rain in 2018," *J. Disaster Res.*, vol. 14, no. 6, pp. 874–885, 2019.
[47] Cabinet Office of Japan, "Damage situation related to the Typhoon No. 19 in 2019," 2020. Accessed: Feb. 14, 2022. [Online]. Available: http://www.bousai.go.jp/updates/r1typhoon19/
[48] "Python software fundation 'Python'," 2022. Accessed: Sep. 10, 2022. [Online]. Available: https://www.python.org/
[49] C. R. Harris et al., "Array programming with NumPy," *Nature*, vol. 585, no. 7825, pp. 357–362, Sep. 2020, doi: 10.1038/s41586-020-2649-2.

Luis Moya received the B.S. and M.S. degrees in civil engineering from the National University of Engineering, Lima, Peru, in 2009 and 2013, respectively, and the Ph.D. degree in engineering from Chiba University, Chiba, Japan, in 2016.

In 2012, he was a Visiting Student with the Building Research Institute, Tsukuba, Japan. From 2016 to 2020, he was a Researcher with the International Research Institute of Disaster Science, Tohoku University, Sendai, Japan. From 2020 to 2022, he was a Researcher with the Japan-Peru for Earthquake Engineering Research and Disaster Mitigation, National University of Engineering. Since 2022, he has been an Assistant Professor with the Department of Engineering, Pontifical Catholic University of Peru, Lima, Peru. His research interests include earthquake engineering, remote sensing for damage assessment, intelligent evacuation systems, and informal urban growth.

Erick Mas was born in Lima, Peru. He graduated from the Faculty of Civil Engineering, National University of Engineering (UNI), Rmac, Peru, the master's degree in disaster risk management from UNI, and the Ph.D. degree from the Graduate School of Engineering and the Faculty of Civil and Environmental Engineering, Tohoku University, Sendai, Japan.

He has professional experience on disaster risk management at regional and local governments in Peru. He also conducted research with Tsunami Engineering Laboratory, Tohoku University. He is currently an Associate Professor with the International Research Institute of Disaster Science (IRIDeS) and appointed to the Tough Cyber Physical AI Research Center, the Co-Creation Center for Disaster Resilience and Technical Advisor to the Rai-Cast Firm. His research interests include agent-based modeling, tsunami risk, evacuation simulation, UAV and remote sensing applications for disaster science.

Shunichi Koshimura received the Ph.D. degree in civil engineering from the Graduate School of Engineering, Tohoku University, Sendai, Japan, in 2000.

He is currently a Professor with the International Research Institute of Disaster Science, Tohoku University. He is also a Cofounder of RTi-cast, a technology firm to offer real-time tsunami inundation damage forecast services to government organizations and commercial clients. His research interests include developing a real-time natural hazard forecast system and on estimating social impacts by integrating numerical modeling, earth observation and geo-informatics.